

# THE TRANSIENT ACCRETING X-RAY PULSAR XTE J1946+274: STABILITY OF X-RAY PROPERTIES AT LOW FLUX AND UPDATED ORBITAL SOLUTION

DIANA M. MARCU-CHEATHAM<sup>1,2</sup>, KATJA POTTSCHMIDT<sup>1,2</sup>, MATTHIAS KÜHNEL<sup>3</sup>, SEBASTIAN MÜLLER<sup>3</sup>, SEBASTIAN FALKNER<sup>3</sup>, ISABEL CABALLERO<sup>4</sup>, MARK H. FINGER<sup>5</sup>, PETER J. JENKE<sup>6</sup>, COLLEEN A. WILSON-HODGE<sup>7</sup>, FELIX FÜRST<sup>8</sup>, VICTORIA GRINBERG<sup>9</sup>, PAUL B. HEMPHILL<sup>10</sup>, INGO KREYKENBOHM<sup>3</sup>, DMITRY KLOCHKOV<sup>11</sup>, RICHARD E. ROTHSCHILD<sup>10</sup>, YUKIKATSU TERADA<sup>12</sup>, TERUAKI ENOTO<sup>13</sup>, WATARU IWAKIRI<sup>14</sup>, MICHAEL T. WOLFF<sup>15</sup>, PETER A. BECKER<sup>16</sup>, KENT S. WOOD<sup>15</sup>, AND JÖRN WILMS<sup>3</sup>

<sup>1</sup>CRESST & Department of Physics, University of Maryland Baltimore County, 1000 Hilltop Circle, Baltimore, MD 21250, USA

<sup>2</sup>NASA Goddard Space Flight Center, Astrophysics Science Division, Greenbelt, MD 20771, USA

<sup>3</sup>Dr. Karl Remeis-Observatory & ECAP, University Erlangen-Nuremberg, Sternwartstr. 7, Bamberg, Germany

<sup>4</sup>Laboratoire AIM, CEA/IRFU, CNRS/INSU, Université Paris Diderot, CEA DSM/IRFU/SAP, F-91191 Gif-sur-Yvette, France

<sup>5</sup>Universities Space Research Association, National Space Science and Technology Center, 320 Sparkman Drive, Huntsville, AL 35805, USA

<sup>6</sup>University of Alabama in Huntsville, 301 Sparkman Drive, Huntsville, AL 35899, USA

<sup>7</sup>Astrophysics Office, ZP 12, NASA Marshall Space Flight Center, Huntsville, AL 35812, USA

<sup>8</sup>Cañill Center for Astronomy and Astrophysics, California Institute of Technology, Pasadena, CA 91125, USA

<sup>9</sup>Massachusetts Institute of Technology, Kavli Institute for Astrophysics, Cambridge, MA 02139, USA

<sup>10</sup>University of California, San Diego, Center for Astrophysics and Space Sciences, 9500 Gilman Drive, La Jolla, CA 92093-0424, USA

<sup>11</sup>Institut für Astronomie und Astrophysik, Universität Tübingen (IAAT), Sand 1, Tübingen, Germany

<sup>12</sup>Graduate School of Science and Engineering, Saitama University, 255 Simo-Ohkubo, Sakura-ku, Saitama City, Saitama 338-8570, Japan

<sup>13</sup>Department of Astronomy and The Hakubi Center for Advanced Research, Kyoto University, Kitashirakawa-Oiwake-cho, Sakyo-ku, Kyoto 606-8502, Japan

<sup>14</sup>RIKEN Nishina Center, 2-1 Hirosawa, Wako, Saitama 351-0198, Japan

<sup>15</sup>Space Science Division, Naval Research Laboratory, Washington, DC, USA

<sup>16</sup>School of Physics, Astronomy, and Computational Sciences, MS 5C3, George Mason University, 4400 University Drive, Fairfax, VA, USA

Received 2015 August 21; accepted 2015 October 16; published 2015 December 8

## ABSTRACT

We present a timing and spectral analysis of the X-ray pulsar XTE J1946+274 observed with *Suzaku* during an outburst decline in 2010 October and compare with previous results. XTE J1946+274 is a transient X-ray binary consisting of a Be-type star and a neutron star with a 15.75 s pulse period in a 172 days orbit with 2–3 outbursts per orbit during phases of activity. We improve the orbital solution using data from multiple instruments. The X-ray spectrum can be described by an absorbed Fermi–Dirac cut-off power-law model along with a narrow Fe K $\alpha$  line at 6.4 keV and a weak Cyclotron Resonance Scattering Feature (CRSF) at  $\sim 35$  keV. The *Suzaku* data are consistent with the previously observed continuum flux versus iron line flux correlation expected from fluorescence emission along the line of sight. However, the observed iron line flux is slightly higher, indicating the possibility of a higher iron abundance or the presence of non-uniform material. We argue that the source most likely has only been observed in the subcritical (non-radiation dominated) state since its pulse profile is stable over all observed luminosities and the energy of the CRSF is approximately the same at the highest ( $\sim 5 \times 10^{37}$  erg s $^{-1}$ ) and lowest ( $\sim 5 \times 10^{36}$  erg s $^{-1}$ ) observed 3–60 keV luminosities.

*Key words:* accretion, accretion disks – pulsars: individual (XTE J1946+274) – X-rays: binaries

## 1. INTRODUCTION

The X-ray pulsar XTE J1946+274 was discovered during a three-month long outburst in 1998 September (Smith & Takeshima 1998) by the All-Sky Monitor on the *Rossi X-Ray Timing Explorer (RXTE)*. Pulsations with a period of 15.83 s were first detected by Wilson et al. (1998) using data from the Burst And Transient Source Experiment (BATSE) on board the *Compton Gamma-Ray Observatory (CGRO)*. XTE J1946+274 was found to be a high-mass X-ray binary (HMXB) with a Be IV/Ive stellar companion (Verrecchia et al. 2002). Wilson et al. (2003) determined an orbital period of 169.2 days, an orbital inclination of  $\sim 46^\circ$ , and a distance of  $9.5 \pm 2.9$  kpc using *RXTE* and BATSE data. Between 1998 and 2001, XTE J1946+274 experienced an outburst approximately every half-orbit: Campana et al. (1999) observed periodic flaring of the X-ray source repeating every  $\sim 80$  days. Between 1999 September and 2000 July, the outbursts were monitored with the Indian X-ray Astronomy Experiment and the data were analyzed by Paul et al. (2001). Paul et al. (2001) and Wilson et al. (2003) presented pulse profiles with double-peaked structures.

The strong magnetic field ( $\sim 10^{12}$  G) of the neutron star enforces collimated accretion along the field lines and quantizes the electron energy states perpendicular to those field lines. When X-ray photons in the column interact through resonant scattering with these quantized electrons they produce an absorption-line-like feature observed in the spectrum at the energy

$$E \approx \frac{11.56 \text{ keV}}{1+z} \left( \frac{B_{\text{NS}}}{10^{12} \text{ G}} \right), \quad (1)$$

where  $B_{\text{NS}}$  is the surface magnetic field and  $z$  is the gravitational redshift, which is  $\sim 0.3$  for typical neutron star parameters, and a line-forming region close to the surface. This is known as a cyclotron resonance scattering feature (CRSF), which, as can be seen in Equation (1), can be used to determine the magnetic field strength of highly magnetized pulsars. The first spectral analysis of XTE J1946+274 was performed by Heindl et al. (2001) using pointed *RXTE* data from the first observed outburst in 1998. They found evidence for a CRSF

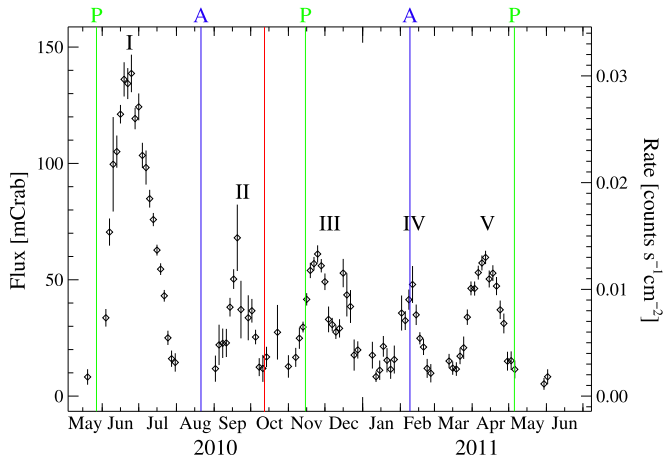


**Figure 1.** *Swift*-BAT 15–50 keV XTE J1946+274 light curve of the series of outbursts in 2010–2011 with a binning of 3 days, showing all bins with  $S/N \gtrsim 2$ ; the vertical red line represents the time of the *Suzaku* observation. The apastron (blue lines marked with “A”) and periastron (green lines marked with “P”) times were determined with the new orbital solution (see Section 3.3). The outbursts are marked I–V. The data were obtained from <http://swift.gsfc.nasa.gov/results/transients/>.

with a centroid energy of  $\sim 36$  keV corresponding to a  $B$  field of  $3.1(1+z) \times 10^{12}$  G.

After 2001 October the source was quiescent until 2010 June. Starting 2010 June 4 the Burst Alert Telescope (BAT) on board *Swift* and the Gamma-ray Burst Monitor (GBM) on board *Fermi* observed a new strong outburst (Finger 2010; Krimm et al. 2010). The BAT light curve (Figure 1) shows that this  $\sim 140$  mCrab outburst was followed by four outbursts at about half the flux at intervals of approximately 82, 75, 73, and 57 days. This behavior is similar to that observed by Campana et al. (1999) for the 1998–2001 outburst series.

Caballero et al. (2010) found no sign of the CRSF at 35 keV in a preliminary analysis of *INTEGRAL* Gamma-Ray Astrophysics Laboratory (*INTEGRAL*) data of the first 2010 outburst. Using *RXTE* and *INTEGRAL* data from the first outburst in 2010 June–July and *Swift*, *RXTE*, and *INTEGRAL* data from the third outburst in 2010 November–December, Müller et al. (2012) reported the possible presence of a CRSF at 25 keV ( $1.81\sigma$  significance).

An iron (Fe)  $K\alpha$  fluorescent line at 6.4 keV is present in the spectra. Müller et al. (2012) reported a correlation between the Fe  $K\alpha$  line flux and the 7–15 keV continuum flux.

In this paper we present a temporal and spectral analysis of *Suzaku* data taken during the end of the second 2010 outburst (red line in Figure 1) that allows for a spectral analysis at the lowest flux to date. Due to its high broadband X-ray sensitivity and its imaging capability, *Suzaku* is an ideal instrument for analyzing broadband spectra and spectral features (iron lines and CRSFs) for sources at very low fluxes. A first temporal and spectral analysis of the same 2010 *Suzaku* data was conducted by Maitra & Paul (2013) who reported the presence of a broad CRSF at  $\sim 38$  keV.<sup>17</sup> The analysis we present here differs significantly from theirs, regarding the spectral analysis itself as well as the breadth of the discussion. The differences between our modeling choices are further explained in Section 4. The

CRSF width of  $\sim 9$  keV found by Maitra & Paul (2013) is rather broad and could indicate a contribution to modeling the continuum (for a demonstration of this effect see Müller et al. 2013b). In addition the source is not consistently detected above 38 keV in all spectral bins, even if broadly rebinned (large uncertainties have also been noted by Maitra & Paul 2013). This is also the reason why we, contrary to Maitra & Paul (2013), do not conduct a pulse phase resolved analysis of the CRSF parameters. Though not excluded, the 38 keV line is thus an unlikely CRSF candidate. As we show in Section 4 there is a possibility that a less broad line is present at  $\sim 35$  keV instead.

The 2010–2011 outburst series was also monitored by *Fermi*-GBM. Together with the available *RXTE*, *Swift*, and *Suzaku* data, these observations allow us to refine the orbit parameters.

In Section 2 we describe the *Suzaku* data and the data reduction procedure, and provide an overview of the additional multi-instrument data used in our analysis. In Section 3 we first examine the *Suzaku* light curves and hardness ratios. We then determine the local pulse period and the energy resolved pulse profiles, which we compare with those observed with *RXTE*-PCA during the bright first outburst of 2010. Last, but not least, we present the improved orbital solution. In Section 4 we present the broadband *Suzaku* spectral analysis. In Section 5 and Section 6 the results are discussed and summarized, respectively.

## 2. OBSERVATIONS AND DATA REDUCTION

We study a  $\sim 50$  ks *Suzaku* observation that occurred on 2010 October 11–13 (ObsID 405041010), during a minimum between the second and third outburst of the 2010 outburst series, when the 15–50 keV flux was  $\sim 10$  mCrab. We extracted data obtained with the X-ray Imaging Spectrometer (XIS, Koyama et al. 2007), and the PIN instrument from the High X-ray Detector (HXD, Takahashi et al. 2007). The three functional units of the XIS (CCD cameras 0, 1, and 3) were operated in the 1/4 window mode during the observation in order to reduce pile-up. Data from the Gadolinium Silicate Crystals (GSO, also part of HXD) were excluded due to the weakness of the source above 40 keV.

We reprocessed the XIS and PIN data and extracted data products following the *Suzaku* Data Reduction (or ABC) Guide (ISAS/JAXA & X-ray Astrophysics Laboratory NASA/Goddard Space Flight Center 2013). The reprocessing was performed using *aepipeline*, applying the newest calibration as well as standard data screening (with the default screening criteria). This was done based on the *HEASOFT* v6.13 software package and the calibration database (*CALDB*) releases HXD-20110913, XIS-20130305, and XRT-20110630. We further filtered the screened XIS events in order to exclude times of telemetry saturation. The events for both XIS and PIN were transferred to the barycenter of the solar system with *aebarycen*.

Using *xselect*, we first extracted XIS images, to which we applied an attitude correction with *aattcor2*, which further corrects the attitude data for thermal wobbling using mean event positions as a function of time. After comparing the images obtained with and without applying *aattcor2*, we concluded that the additional attitude correction does not improve the moderate systematic attitude instability that is visible in the images through an elongated and double-peaked

<sup>17</sup> Note that Maitra & Paul (2013) quote the resonance energy of a pseudo-Lorentzian line shape; the energy of the minimum of the line shape that is comparable to the CRSF energy values quoted elsewhere in this paper is  $\sim 40$  keV (see page 94 of Mihara 1995, and Enoto et al. 2008).

point-spread function (PSF; see Maeda 2010a, 2010b, 2010c for further discussions of this effect). As we will show in Section 3.1, the systematic attitude wobble has a negligible effect on the spectral shape.

XIS source and background event files, light curves, and spectra were produced using `xselect` after selecting the extraction regions in the XIS image. For bright sources, this step involves the determination of possibly existing pile up using `pileest`. For XTE J1946+274 the pile up fraction was <4% in the center of the PSF, thus the source was not bright enough to cause strong pile up during this observation. We used the same source extraction region for the three XIS units and the two editing modes alternately used for event storage (“3 × 3” and “5 × 5”): a circle with a radius of 120 pixels (124.8) centered on the PSF. The circle is large enough to contain most of the source events, but not larger than the window. The background regions were circles with radii of 95 pixels (98.8), located within the windows, but as far from the PSFs as possible. XIS 0 has a strip of unusable, masked pixels near the edge of the detector and therefore our XIS 0 background region additionally avoided this zone (Tsujiyama et al. 2010).

The XIS source and background light curves were extracted with 128 s resolution in the energy bands 0.5–5 keV, 5–10 keV, and 0.5–10 keV. Since the orbital period of the neutron star (172 days) is significantly larger than the duration of the observation (50 ks), we did not perform a binary star orbit correction. The XIS spectra were binned to a resolution close to the half-width half-maximum of the spectral resolution of the instrument (Nowak et al. 2011). To generate the energy and ancillary responses we used the `xismfgen` and `xissimarfgen` tools, respectively. The exposure time for each XIS CCD is ~50 ks, while the average source count rates are ~3.05 counts s<sup>-1</sup> for XIS 0, ~2.80 counts s<sup>-1</sup> for XIS 1, and ~3.48 counts s<sup>-1</sup> for XIS 3.

For PIN we applied energy filtering (10–20 keV, 20–40 keV, 40–70 keV, and 10–70 keV) to the event files obtained after running `aepipeline`, after which we extracted light curves with `hxdpinxblc` with a time binning of 128 s. This tool produces the total dead-time corrected PIN light curve, the non-X-ray background (NXB) light curve, and the background-subtracted source light curve. We used `hxdpinxbpi` for the PIN spectral extraction which provides the dead-time corrected PIN source spectrum and the NXB and Cosmic X-ray Background (CXB) spectra. Approximately 5% of the PIN background is CXB and the corresponding spectrum is simulated based on the description by Boldt (1987). The NXB light curve and spectrum produced by the extraction tools are based on modeled events available for each individual observation.<sup>18</sup> For the spectral modeling we used the summed NXB and CXB background. The appropriate response file for the specific calibration epoch was chosen (`ae_hxd_pinhx_nome9_20100731.rsp`). For the PIN spectra we applied a binning of a factor of 2 for the energy range 34–40 keV. The exposure time for PIN is ~43 ks, while the total average source count rate is ~0.90 counts s<sup>-1</sup>.

In addition to these *Suzaku* data we also used XTE J1946+274 data from other instruments. The pulse profile comparison in Section 3.2 presents the *Suzaku*-XIS and *Suzaku*-PIN data together with *RXTE*-PCA data from the peak of the first

**Table 1**  
Observations

Satellite Instrument	Observation Time	Number of Observations Total Exposure Time
<i>Fermi</i> GBM	2010 Dec 16–2011 May 1 1st–5th outbursts in 2010	monitoring
<i>RXTE</i> PCA, HEXTE <sup>a</sup>	1998 Sep 16–1998 Oct 14 1st outburst in 1998	12 observations ~30 ks
<i>RXTE</i> PCA <sup>b</sup>	2010 Jun 20–2010 Jul 16 1st outburst in 2010	17 observations ~60 ks
<i>RXTE</i> PCA <sup>b</sup>	2010 Nov 23–2010 Dec 07 3rd outburst in 2010	9 observations ~23 ks
<i>Swift</i> XRT <sup>b</sup>	2010 Nov 26–2010 Dec 28 3rd outburst in 2010	8 observations ~16 ks
<i>INTEGRAL</i> ISGRI <sup>b</sup>	2010 Jun 20–2010 Nov 30 1st & 4th outbursts in 2010	5 observations ~150 ks
<i>Suzaku</i> XIS, PIN <sup>c</sup>	2010 Oct 11–13 end of 2nd outburst in 2010	1 observation ~50 ks

**Notes.**

<sup>a</sup> Heindl et al. (2001, their Table 1).

<sup>b</sup> Müller et al. (2012, first sentence of notes on their Table 1).

<sup>c</sup> This work (Section 2).

outburst in 2010. The orbit determination in Section 3.3 is based on the complete 2010 outburst series. The majority of pulse period measurements is provided by the *Fermi*-GBM Pulsar Project<sup>19</sup> while also including *Suzaku*-PIN, all available *RXTE*-PCA, and *Swift*-XRT data. In Section 5 we compare *Suzaku* results with results from Heindl et al. (2001) and Müller et al. (2012) obtained with *RXTE*, *Swift*, and *INTEGRAL*. For all observations used in our analysis, the instruments that performed them, their observation times, and their exposure times are listed in Table 1.

### 3. TEMPORAL ANALYSIS

#### 3.1. *Suzaku* Light Curves and Hardness Ratios

Figures 2(a) and (b) show the background-subtracted light curves for the summed count rates of XIS 0, 1, and 3 (0.5–10 keV) and for the PIN count rate (10–70 keV), respectively. According to the *Swift*-BAT light curve in Figure 1, the *Suzaku* observation was performed at the end of a decreasing long-term flux trend. This appears to be consistent with the PIN light curve, which might show a moderate decline from  $1.06 \pm 0.03$  counts s<sup>-1</sup> in the first satellite orbit of the observation to  $0.86 \pm 0.03$  counts s<sup>-1</sup> in the last one. There are no significant flares or dips observed. The XIS light curve displays jumps between two count rate levels for most *Suzaku* orbits. The effect can be observed in all three XIS units individually, and it is consistent with the systematic attitude instability mentioned in Section 2. This is aggravated by the HXD aim-point used for this observation, since it is slightly off-center on the XIS chips.

Figures 2(c) and (d) show hardness ratio evolutions for count rates in the energy bands 5–10 keV and 0.5–5 keV and for count rates in the energy bands 10–20 keV and 0.5–5 keV,

<sup>18</sup> [http://legacy.gsfc.nasa.gov/suzaku/data/background/pinxb\\_ver2.0\\_tuned/2010\\_10/ae405041010\\_hxd\\_pinbgd.evt.gz](http://legacy.gsfc.nasa.gov/suzaku/data/background/pinxb_ver2.0_tuned/2010_10/ae405041010_hxd_pinbgd.evt.gz)

<sup>19</sup> <http://gamma-ray.nsstc.nasa.gov/gbm/science/pulsars/>

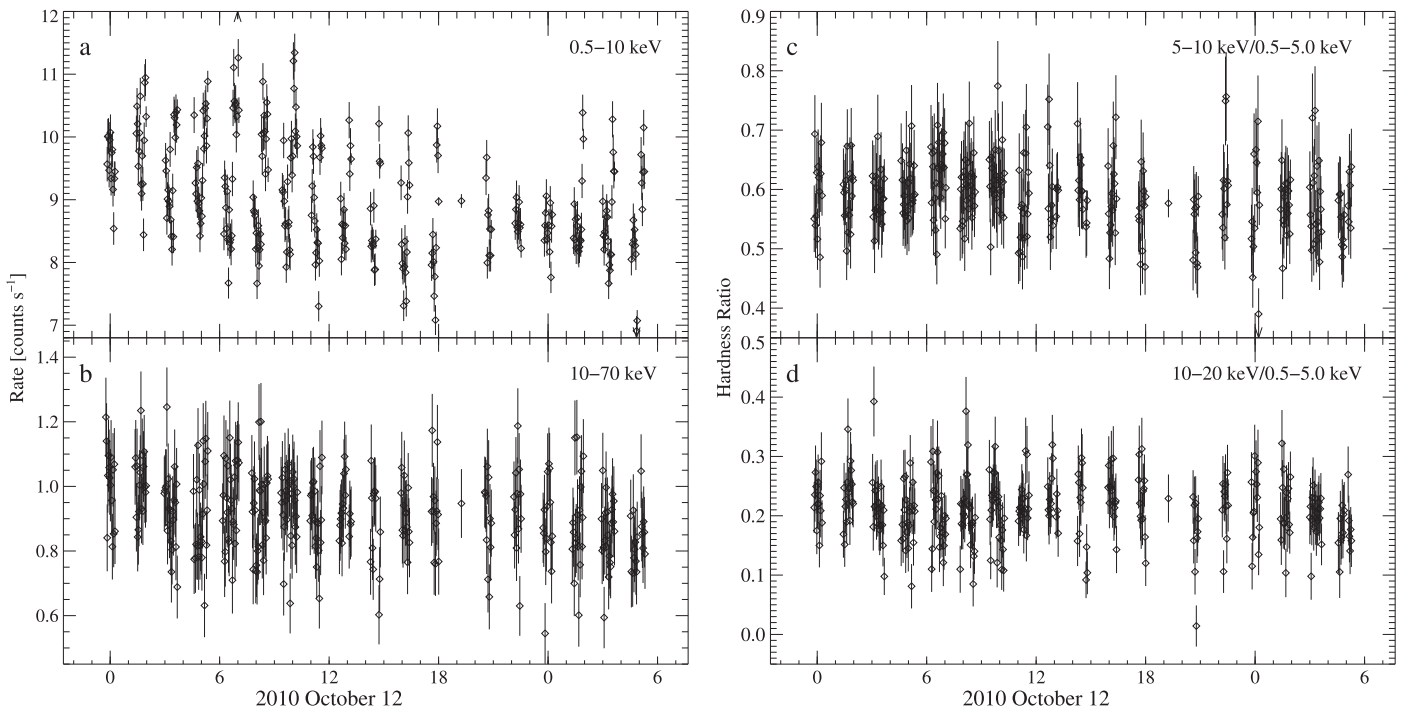


**Figure 2.** (a) Light curve of summed XIS 0, 1, and 3 count rates (0.5–10 keV). (b) Dead-time corrected PIN light curve (10–70 keV). Both light curves are background subtracted and binned to 128 s. (c) Hardness ratio evolution for count rates in the energy bands 5–10 keV and 0.5–5 keV using XIS 3. (d) Hardness ratio evolution for count rates in the energy bands 10–20 keV and 0.5–5 keV using PIN and XIS 3.

respectively. We observe little structure related to the systematic attitude instability in the XIS-PIN band ratios, and no structure in the XIS-XIS band ratios. Since there are no significant source related flux or hardness changes over the observation, we do not perform a time-resolved spectral analysis, but model the observation averaged spectra in Section 4.

### 3.2. Pulse Period and Pulse Profiles

The XIS has a time resolution of 2 s when in 1/4 window mode, while the PIN has a resolution of 61  $\mu$ s (ISAS/JAXA & X-ray Astrophysics Laboratory NASA/Goddard Space Flight Center 2015). Therefore, only the PIN data were used for the pulse period determination. Applying epoch folding (Leahy et al. 1983; Schwarzenberg-Czerny 1989) to the screened, barycenter-corrected, non-background-subtracted PIN events, in the 10–40 keV range, we determined a local pulse period of 15.750025(27) s. The uncertainty was estimated using Monte Carlo light curve simulations as described in Section 3.3.

Based on this period and a reference time of MJD 55481.714 for phase 0, we obtained pulse profiles in several energy bands by folding the screened, barycenter-corrected events using 8 phase bins for XIS (0.5–5 keV and 5–10 keV; note that the *Suzaku*-XIS pulse profiles presented by Maitra & Paul (2013) are oversampled) and 128 phase bins for PIN (10–20 keV, 20–40 keV and 40–70 keV). Figure 3 shows that up to 40 keV the pulse profiles are consistent in general structure: they are double-peaked, with a deep ( $\phi \sim 0.35$ ) and a shallow minimum ( $\phi \sim 0.9$ ). In the 10–20 keV range an additional narrow peak feature is visible ( $\phi \sim 0.2$ ) before the deep minimum. The shallow minimum is deeper at energies  $\lesssim 5$  keV than at higher energies. Similar behavior was found by Wilson

et al. (2003) during two outbursts observed with *RXTE*-PCA in 1998 and 2001. We determined the pulse fractions measured with PIN as the difference between the maximum and minimum count rates of the profiles normalized by mean count rate, and obtained values of  $1.02 \pm 0.09$  and  $1.04 \pm 0.12$  for the 10–20 keV and 20–40 keV energy ranges, respectively. Wilson et al. (2003) found pulsed fractions as high as 0.74 in the 2–30 keV range during low-flux outbursts in 2001. No pulsations are visible in the 40–70 keV *Suzaku* profile.

Figures 3(c) and (d) include a comparison for the 10–20 keV and 20–40 keV energy bands between the *Suzaku*-PIN pulse profiles from 2010 October 12 (end of the second outburst) and the *RXTE*-PCA pulse profiles from 2010 June 26 (ObsID 95032-12-02-00, peak of the first outburst). The latter were obtained using the same light curve extraction criteria as Müller et al. (2012) used for the full PCA energy band and applying epoch folding with the local period of 15.764 s determined by their analysis. This comparison emphasizes that the shapes of the profiles obtained from the two instruments are very similar, especially at higher energies, despite the large difference in flux:

$$\begin{aligned}
 10\text{--}20 \text{ keV flux} &: \begin{cases} 1.57 \times 10^{-9} \text{ erg s}^{-1} \text{ cm}^{-2} & \text{PCA,} \\ 2.10 \times 10^{-10} \text{ erg s}^{-1} \text{ cm}^{-2} & \text{Suzaku,} \end{cases} \\
 20\text{--}40 \text{ keV flux} &: \begin{cases} 1.12 \times 10^{-9} \text{ erg s}^{-1} \text{ cm}^{-2} & \text{PCA,} \\ 1.30 \times 10^{-10} \text{ erg s}^{-1} \text{ cm}^{-2} & \text{Suzaku.} \end{cases}
 \end{aligned}$$

The *Suzaku* fluxes were derived from the spectral best-fit model presented in Section 4.1 and the *RXTE*-PCA fluxes from the spectral best fit of the averaged observations during the peak of the first outburst (epoch 1 fit of Müller et al. 2012).

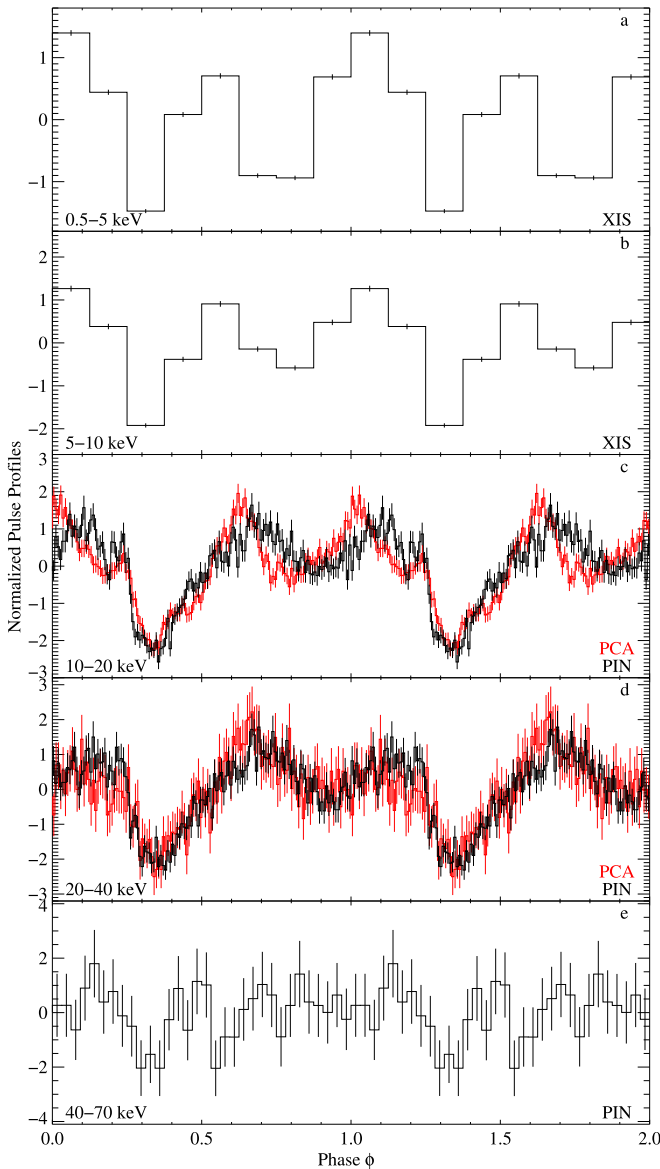


**Figure 3.** Energy-resolved *Suzaku* and *RXTE* pulse profiles for the respective instruments and energy ranges: (a) XIS 3, 0.5–5 keV, (b) XIS 3, 5–10 keV, (c) PIN (in black) and PCA (in red), 10–20 keV, (d) PIN and PCA, 20–40 keV, (e) PIN, 40–70 keV. The *RXTE*-PCA pulse profiles are from the peak of the bright first outburst in 2010 June (see Section 3.2 for further discussion). The number of phase bins for XIS, PIN, and PCA is 8, 128, and 128, respectively, with the exception of 32 for the 40–70 keV PIN range. The period values the *Suzaku* and *RXTE* events were folded on are 15.750025s (this work) and 15.764 s (Müller et al. 2012), respectively. The profiles were normalized to show standard deviations above the mean.

### 3.3. Orbit Determination

The observed pulse period over time as measured by an observer is due to the intrinsic spin-up or spin-down of the neutron star, caused, e.g., by accretion torques, and on due to the Doppler shift by orbital motion. Usually the Doppler shift dominates changes in the measured pulse period. For XTE J1946+274, however, the neutron star undergoes a strong spin-up during outbursts such that the orbital parameters of the system could not be constrained well in the past.

Wilson et al. (2003) were able to describe the pulse frequencies as measured by *CGRO*-BATSE and *RXTE*-PCA during the outburst series between 1998 and 2001 using a

piecewise linear approximation of the intrinsic spin-up. Their best fit with a  $\chi^2_{\text{red}} = 5.94$  for 37 degrees of freedom (dof) shows that this simplified approximation cannot give a good description of the measured period evolution.

In the most simple model for the angular momentum transfer of the infalling material onto the neutron star (Ghosh & Lamb 1979), the period change of the neutron star is connected to the luminosity  $L$  via

$$-\dot{P} \propto P^2 L^\alpha \quad (2)$$

where  $\alpha = 1$  for wind and  $\alpha = 6/7$  for disk accretion. Assuming that the luminosity of the source is proportional to the measured flux  $F$ , the pulse period at the time  $t$  is then given by

$$P(t) = P_0 + a(t - t_0) - b \int_{t_0}^t \left( \frac{P(t')}{P_0} \right)^2 \left( \frac{F(t')}{F_{\text{ref}}} \right)^\alpha dt', \quad (3)$$

where  $P_0$  is the pulse period at the reference time,  $t_0$ ,  $b$  is the torque strength, and  $F_{\text{ref}}$  is a reference flux. The model also takes a constant spin change,  $a$ , into account, which could be caused by, e.g., the propeller effect (Illarionov & Sunyaev 1975). We obtain the observed pulse period  $P_{\text{obs}}(t)$  by applying the Doppler shift caused by the orbital motion to  $P(t)$  as defined in Equation (3):

$$P_{\text{obs}} = P(t)(1 + v(t)/c), \quad (4)$$

where  $v(t)$  is the orbital velocity of the neutron star projected on the line of sight and  $c$  is the speed of light. The orbital parameters needed to calculate  $v(t)$  are the orbital period,  $P_{\text{orb}}$ , the time of periastron passage,  $\tau$ , the projected semimajor axis,  $a_{\text{sm}} \sin i$ , where  $i$  is the inclination, the eccentricity  $e$ , and the longitude of periastron  $\omega$ , such that

$$v(t) = \frac{2\pi a_{\text{sm}} \sin i}{P_{\text{orb}}(1 - e^2)^{1/2}} (\cos(\theta(t) + \omega) + e \cos \omega), \quad (5)$$

where  $\theta(t)$  is the true anomaly found by solving Kepler's equation, which itself depends on the orbital parameters listed above.

During the activity of XTE J1946+274 in 2010 and 2011, various X-ray and gamma-ray missions observed the source (see Section 2 and Table 1 for details), such that the pulse period evolution is known in great detail especially from *Fermi*-GBM. We searched for pulsations near the GBM period for *Suzaku*-PIN, *RXTE*-PCA, and *Swift*-XRT using the epoch folding technique. For the PIN we determined a pulse period of 15.750025(27) s, see Section 3.2. For PCA, we used PCU2 top-layer light curves, extracted in GoodXenon mode with a time resolution of 0.125 s. The XRT data were taken in Windowed Timing mode. The XRT light curves were obtained from a  $\sim 0.5$  region centered on the source position and rebinned to a 1 s time resolution. The initial uncertainties of the measured pulse periods were estimated by Monte Carlo simulations, where synthetic light curves of the source based on the observed pulse profile were searched for the pulse period. The uncertainties of the periods measured by *Fermi*-GBM were provided by the GBM Pulsar Project. The measured pulse periods of XTE J1946+274 are shown in Figure 4.

In order to compute the pulse periods via Equation (3), we used the 1 day binned 15–50 keV *Swift*-BAT light curve of the source as the bolometric flux evolution  $F(t)$  and chose

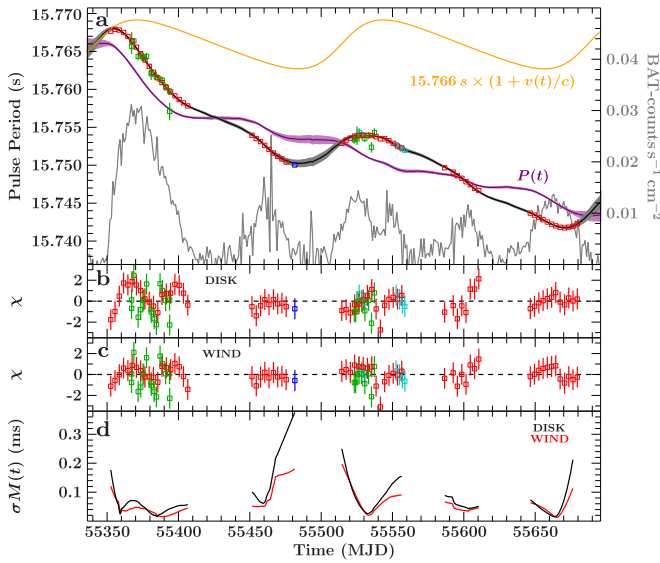


**Figure 4.** Orbit determination: the upper panel (a) shows the observed evolution of barycenter-corrected pulse period values obtained with *Fermi*-GBM (red squares), *Suzaku*-PIN (dark blue square), *RXTE*-PCA (green squares), and *Swift*-XRT (light blue squares). It also shows the overall modeled pulse period evolution (black), the modeled intrinsic spin period evolution (purple), and the orbital motion effect (orange) for the DISK model. The BAT 15–50 keV light curve is overplotted in gray. The lower panels show the residuals for fitting (b) the DISK model and (c) the *WIND* model to the observed evolution. Both models include intrinsic and orbital effects, but differ in the choice of the luminosity exponent  $\alpha$ . The model uncertainties are taken into account in the residuals and in the overall model and intrinsic spin period evolution drawn as a band in lighter colors. Panel (d) shows the Monte Carlo simulation of the model uncertainties: as described in the text, the *Swift*-BAT light curve was randomized within its uncertainties, resulting in a different best fit of Equation (4) to the pulse periods during each run. The standard deviation of all calculated pulse period evolutions at the times where period measurements are available is shown for different assumptions of  $\alpha$  in black (DISK) and red (*WIND*). These values are interpreted as model uncertainties for the final fits.

$F_{\text{ref}} = 1 \text{ count s}^{-1} \text{ cm}^{-2}$ . Using the hard BAT flux as a proxy for the bolometric flux is justified since the source does not show strong spectral changes over and between outbursts (Müller et al. 2012, this work). The main source of uncertainty in the predicted pulse period therefore does not come from changes in the spectral shape, but from the overall uncertainty in the BAT flux measurements, which can have uncertainties of up to 15%. In order to take these uncertainties into account, we use a Monte Carlo approach in which 10,000 BAT light curves are simulated. For each time with a BAT measurement,  $t_i$ , we draw a simulated BAT count rate from a Gaussian distribution with mean and standard deviation given by the measured BAT rate and uncertainty, respectively. For each of the light curve realizations we then derive the best-fit pulse period evolution using Equation (4). The standard deviation of the resulting simulated pulse periods,  $\sigma_{M(t_i)}$ , at each  $t_i$  is then taken to be representative of the uncertainty of the modeled pulse period evolution.

In order to obtain the final orbit and pulse period model, based on an initial estimate for  $\sigma_{M(t_i)}$  we minimize the fit statistics

$$\chi^2 = \sum_i \frac{(P_i - P_{\text{obs}}(t_i))^2}{\sigma_{P_i}^2 + \sigma_{M(t_i)}^2}, \quad (6)$$

**Table 2**  
Orbital Parameters and Spin Period Evolution; Uncertainties Are on the 90% Confidence Level

	DISK	WIND
$a_{\text{sm}} \sin i$ (lt-s)	$471.2^{+2.6}_{-4.3}$	$471.1^{+2.7}_{-2.8}$
$P_{\text{orb}}$ (days)	$172.7^{+0.6}_{-0.6}$	$171.4^{+0.4}_{-0.4}$
$\tau$ (MJD)	$55514.8^{+0.8}_{-1.1}$	$55515.5^{+0.8}_{-0.7}$
$e$	$0.246^{+0.009}_{-0.009}$	$0.266^{+0.007}_{-0.007}$
$\omega$ ( $^\circ$ )	$-87.4^{+1.5}_{-1.7}$	$-87.1^{+1.2}_{-1.0}$
$t_0$	55550 (fixed)	55550 (fixed)
$P_0$ (s)	$15.749742^{+0.000023}_{-0.000014}$	$15.749753^{+0.000013}_{-0.000013}$
$a$ ( $\text{s s}^{-1}$ )	$1.67^{+0.16}_{-0.18} \times 10^{-10}$	$0.47^{+0.20}_{-0.10} \times 10^{-10}$
$b$ ( $\text{s s}^{-1}$ )	$6.52^{+0.06}_{-0.08} \times 10^{-8}$	$10.76^{+0.05}_{-0.04} \times 10^{-8}$
$\alpha$	6/7 (fixed)	1 (fixed)
$\chi^2_{\text{red}}/\text{dof}$	1.05/89	1.06/89

**Note.** Listed are the projected semimajor axis,  $a_{\text{sm}} \sin i$ , the orbital period,  $P_{\text{orb}}$ , the time of periastron passage,  $\tau$ , the eccentricity,  $e$ , the longitude of periastron,  $\omega$ , the reference time,  $t_0$ , the spin period at  $t_0$ ,  $P_0$ , the constant spin change,  $a$ , the torque strength,  $b$ , and the luminosity exponent,  $\alpha$ .

where  $P_i$  is the measured pulse period at time  $t_i$ ,  $P_{\text{obs}}(t_i)$  is the model period (Equation (4)), and  $\sigma_{P_i}$  and  $\sigma_{M(t_i)}$  are the uncertainties of the data and the model as described above. We then iteratively apply the Monte Carlo approach above to refine the estimated model uncertainties. Usually three iterations are sufficient to obtain convergence. Figure 4(d) displays the final estimate for the uncertainty of the pulse period model.

Fits to Equation (4) are shown in Figure 4. The modeled intrinsic spin period  $P(t)$  of the neutron star (shown in purple) dominates the period evolution (black) compared to the effect of the orbital motion (orange). The two residual panels show different assumptions for the exponent  $\alpha$  of Equation (2). In order to check the dependency of the orbital parameters on the assumed torque model, we model the data for both,  $\alpha = 6/7$  (the DISK model) and for  $\alpha = 1$  (the *WIND* model). As illustrated by Figure 4, both models result in a successful description of the measured pulse period evolution and yield *orbital* parameters that are consistent with each other (Table 2).

We stress again that for each of the two models the additional uncertainties due to the BAT data have to be calculated separately by the iterative Monte Carlo approach described above. The resulting uncertainties of the model vary between 0.02 and 0.38 ms with a mean of 0.09 ms (see Figure 4(d)). Within the model uncertainties, however, the model pulse periods agree with the measured data. For example, the pulse period predicted by the DISK model for the time of the *Suzaku* observation is 15.750300(380) s, while the observed period is 15.750025(27) s. Unfortunately, the model uncertainty is large enough that it is not possible for us to distinguish between the different torquing models, with both model fits yielding almost the same  $\chi^2$ . Thankfully, as shown in Table 2, the orbital parameters are insensitive to the details of modeling  $\dot{P}(t)$ . It is only the best-fit values for the spin change,  $a$ , and the torque strength,  $b$ , that differ significantly. Numerical experimenting revealed that this is due to a strong parameter degeneracy of the luminosity exponent  $\alpha$  with  $a$  and

b. Based on the pulse period evolution alone it is therefore not possible to distinguish between the two torquing scenarios.

#### 4. SPECTRAL ANALYSIS

##### 4.1. Best-fit Model

We modeled the 1–9.4 keV XIS and the 17–38 keV PIN spectra using `xspec12` (Arnaud 1996). The 1.8–2.4 keV range was excluded due to known calibration uncertainties (ISAS/JAXA & X-ray Astrophysics Laboratory NASA/Goddard Space Flight Center 2013). We applied the normalization constants  $c_{\text{XIS } 1}$ ,  $c_{\text{XIS } 3}$ , and  $c_{\text{PIN}}$  to account for the flux cross-calibration between the respective instruments relative to XIS 0, where  $c_{\text{XIS } 0}$  was fixed at 1 (`xspec model constant`). The absorption was modeled with `tbnew`, an updated version of `tbabs`,<sup>20</sup> using cross sections by Verner & Yakovlev (1995) and abundances by Wilms et al. (2000). Extending the fit down to 0.8 keV, Maitra & Paul (2013) included an additional partial covering absorption component. Since they found that its parameters are model dependent and since the hardness ratio evolution over the observation (Figures 2(c) and (d)) does not indicate any variability due to partial covering, we used one fully covering absorber alone sufficient which is to model the data down to 1 keV well.

Following the spectral analysis of Müller et al. (2012), we first fitted a Fermi–Dirac cut-off model (`powerxfdcut`, Tanaka 1986), described by:

$$M_{\text{FDCUT}}(E) \propto E^{-\Gamma} \times \left[ 1 + \exp\left(\frac{E - E_{\text{cut}}}{E_{\text{fold}}}\right) \right]^{-1}, \quad (7)$$

where the photon flux at energy  $E$  is described by a power law with a photon index  $\Gamma$ , multiplied by an exponential cut off at energy  $E_{\text{cut}}$  with a folding energy  $E_{\text{fold}}$ . The soft Galactic ridge emission seen in the 6–7 keV range, which needed to be taken into account for PCA data modeling by Müller et al. (2012), is not required for *Suzaku* due to XIS being an imaging instrument. The results of this fit are listed in Table 3 in the column labeled FDCUT I. Figure 5(b) shows the residuals from fitting the continuum model only.

The strongest residuals are seen at 6.41 keV. We interpreted this as a narrow Fe  $K\alpha$  fluorescence line that we proceeded to describe with a Gaussian line model (`Gaussian`). The width is unresolved and we fixed it at  $\sigma_{\text{Fe}} = 0.1$  keV, slightly below the XIS detector resolution. The results of this fit are listed in Table 3 in the column labeled FDCUT II and Figure 5(c) shows the fit residuals.

Residuals are still visible in the PIN energy range, especially around 35 keV. We included an absorption-like line with a Gaussian optical depth profile (`gabs`) often used to describe cyclotron lines:

$$M_{\text{CRSF}}(E) = \exp(-\tau(E)) \quad (8)$$

with

$$\tau(E) = \tau_{\text{CRSF}} \exp\left[-\frac{1}{2}\left(\frac{E - E_{\text{CRSF}}}{\sigma_{\text{CRSF}}}\right)^2\right] \quad (9)$$

where  $E_{\text{CRSF}}$  is the cyclotron line energy,  $\sigma_{\text{CRSF}}$  is the line width, and  $\tau_{\text{CRSF}}$  is the optical depth. Note that the `gabs` implementation

provides the line depth  $D_{\text{CRSF}} = \tau_{\text{CRSF}} \sigma_{\text{CRSF}} \sqrt{2\pi}$  instead of  $\tau_{\text{CRSF}}$ . The CRSF width was unresolved and we fixed it at  $\sigma_{\text{CRSF}} = 2$  keV, close to PIN’s detector resolution. The results of this fit are listed in Table 3 in the column labeled FDCUT III. Figure 5(a) shows the spectra and fitted model and Figure 5(e) shows the fit residuals. The latter do not show any further strong features. In order to illustrate the contribution of the CRSF feature to the best fit, Figure 5(d) shows the residuals of the best fit with the CRSF depth set to 0. We tried fixing the PIN cross normalization constant to its canonical value of 1.181 for an HXD-nominal pointing position (Maeda et al. 2008). This resulted in a worse fit with  $\chi_{\text{red}}^2 = 1.35$ , therefore, we left  $c_{\text{PIN}}$  free.

We then checked whether the presence of a “10 keV feature” is consistent with the data. This is a broad residual that has been observed in the spectra of several accreting pulsars thought to be caused by imperfect modeling of the continuum shape using empirical models (see, e.g., Coburn et al. 2002). It is generally detected as a positive residual (e.g., in Cen X-3, see Suchy et al. 2008) but in some sources, including XTE J1946+274, it appears as a negative one (e.g., in Vela X-1, see Fürst et al. 2014). We applied the deeper of the two detections reported for XTE J1946+274 by Müller et al. (2012) to our model, i.e., following them, we included a `gauabs` component (another parameterization of the `gabs` shape) with  $E_{10\text{keV}} = 9.85$  keV,  $\sigma_{10\text{keV}} = 2.2$  keV, and  $\tau_{10\text{keV}} = 0.069$ . This approach did not significantly change the quality of the fit and fitting  $\tau_{10\text{keV}}$  resulted in a value consistent with 0. We conclude that such a component could be present in the spectrum but is not detected, probably in part due to the lack of data between 9.4 and 17 keV.

Our `fdcut` based best-fit model (FDCUT III) thus consists of absorption in the interstellar medium as well as intrinsic to the system, a power-law continuum with a rollover, a Gaussian emission line for Fe  $K\alpha$  fluorescence, and an absorption-like line with a Gaussian optical depth profile for the cyclotron line:

$$M_{\text{best}}(E) = \text{const} \times \text{tbnew} \times (\text{power} \times \text{fdcut} + \text{Gauss}) \times \text{gabs} \quad (10)$$

in `xspec` notation. We obtain an unabsorbed 3–60 keV flux of  $4.40 \pm 0.01 \times 10^{-10} \text{ erg s}^{-1} \text{ cm}^{-2}$ .

In the following we present results replacing the `powerxfdcut` continuum with other continuum models commonly applied to accreting X-ray pulsars (see, e.g., Müller et al. 2013b, for the equations describing these models): a power law with an exponential cut off (`cutoffpl`), a power law with a high energy cut off (`powerxhighcut`, sometimes also called `plcut`), and the sum of a negative and a positive power law with an exponential cut off (`npex`, Mihara 1995). The last three columns of Table 3 show the best-fit spectral parameters using these continuum models. Since the fitted values of the cut-off energy of `highcut` and the normalization of the positive power law of `npex` are consistent with 0 these three models are degenerate and result in the same fit quality and in the same values of their common parameters. The `fdcut` fit has a slightly different rollover shape, but its parameters are also qualitatively, and often quantitatively within errors, the same. We note that the `npex` parameters reported by Heindl et al. (2001) for the bright outburst of 1998, which were obtained fitting averaged *RXTE* monitoring spectra above 8 keV, can also describe the PIN

<sup>20</sup> <http://pulsar.sternwarte.uni-erlangen.de/wilms/research/tbabs/>

**Table 3**  
Spectral Fit Parameters

	FDCUT I	FDCUT II	FDCUT III	CUTOFFPL	HIGHECUT	NPEX <sup>b</sup>
$N_{\text{H}} (\times 10^{22} \text{ cm}^{-2})$	$1.14^{+0.01}_{-0.02}$	$1.66^{+0.02}_{-0.03}$	1.67(3)	$1.59^{+0.02}_{-0.04}$	$1.59^{+0.02}_{-0.04}$	$1.58^{+0.03}_{-0.05}$
$A_{\text{F}} (\times 10^{-2} \text{ keV}^{-1} \text{ cm}^{-2} \text{ s}^{-1})$	$2.04^{+0.03}_{-0.05}$	$2.02^{+0.03}_{-0.05}$	$2.05^{+0.04}_{-0.05}$	0.97(2)	0.97(2)	$0.96^{+0.02}_{-0.04}$
$\Gamma$	$0.55^{+0.01}_{-0.02}$	$0.55^{+0.01}_{-0.02}$	0.57(2)	$0.41^{+0.02}_{-0.04}$	$0.41^{+0.02}_{-0.04}$	$0.39^{+0.04}_{-0.08}$
$E_{\text{fold}}$ (keV)	$8.6^{+0.2}_{-0.3}$	$8.5^{+0.2}_{-0.3}$	$8.9^{+0.4}_{-0.4}$	$9.6^{+0.4}_{-0.6}$	$9.6^{+0.4}_{-0.6}$	$9.1^{+0.8}_{-1.4}$
$E_{\text{cut}} (\times 10^{-2} \text{ keV})$	$0.09^{+0.04}_{-0.09}$	$0.01^{+0.00}_{-0.01}$	$0.05^{+0.03}_{-0.05}$	...	$0.01^{+0.00}_{-0.01}$	...
$\Gamma_2$	...	...	...	...	...	$-2^{\text{a}}$
$\alpha (\times 10^{-2})$ (keV/keV)	...	...	...	...	...	$0.020^{0.003}_{-0.020}$
$E_{\text{Fe}}$ (keV)	...	6.41(3)	6.41(3)	6.41(3)	6.41(3)	6.41(3)
$\sigma_{\text{Fe}}$ (keV)	...	0.1 <sup>a</sup>				
$A_{\text{Fe}} (\times 10^{-5} \text{ photons cm}^{-2} \text{ s}^{-1})$	...	$8.6^{+1.3}_{-1.4}$	$8.6^{+1.3}_{-1.3}$	$8.7^{+1.3}_{-1.4}$	$8.7^{+1.3}_{-1.4}$	$8.7^{+1.1}_{-1.0}$
$E_{\text{CRSF}}$ (keV)	...	...	$35.2^{+1.5}_{-1.3}$	$34.8^{+1.2}_{-1.0}$	$34.8^{+1.2}_{-1.0}$	$34.8^{+1.1}_{-1.0}$
$\sigma_{\text{CRSF}}$ (keV)	...	...	2 <sup>a</sup>	2 <sup>a</sup>	2 <sup>a</sup>	2 <sup>a</sup>
$D_{\text{CRSF}}$ (keV)	...	...	$2.4^{+1.5}_{-1.3}$	$3.5^{+1.5}_{-1.5}$	$3.5^{+1.5}_{-1.5}$	$3.8^{+1.6}_{-1.5}$
$c_{\text{XIS } 0}$	1 <sup>a</sup>					
$c_{\text{XIS } 1}$	1.07(1)	1.07(1)	1.07(1)	1.07(1)	1.07(1)	1.07(1)
$c_{\text{XIS } 3}$	0.95(1)	0.95(1)	0.95(1)	0.95(1)	0.95(1)	0.95(1)
$c_{\text{PIN}}$	$1.32^{+0.07}_{-0.05}$	$1.35^{+0.07}_{-0.05}$	$1.29^{+0.07}_{-0.06}$	$1.29^{+0.07}_{-0.05}$	$1.29^{+0.08}_{-0.05}$	$1.31^{+0.07}_{-0.06}$
$\chi^2_{\text{red}}/\text{dof}$	1.38/470	1.19/468	1.17/466	1.12/467	1.12/466	1.12/466

**Notes.** The XIS and PIN spectra were fitted simultaneously with the models described in Section 4.1. The columns are labeled according to the continuum that was used. The uncertainties are given on a 90% confidence level.

<sup>a</sup> These parameters were frozen while fitting.

<sup>b</sup> For the model  $M_{\text{NPEX}}(E) \propto (E^{-\Gamma} + \alpha E^{\Gamma_2})e^{-E/E_{\text{fold}}}$  the parameters  $\Gamma$  and  $\Gamma_2$  are the indices of the falling and rising power-law components and  $\alpha$  is the normalization of the rising relative to the falling component.

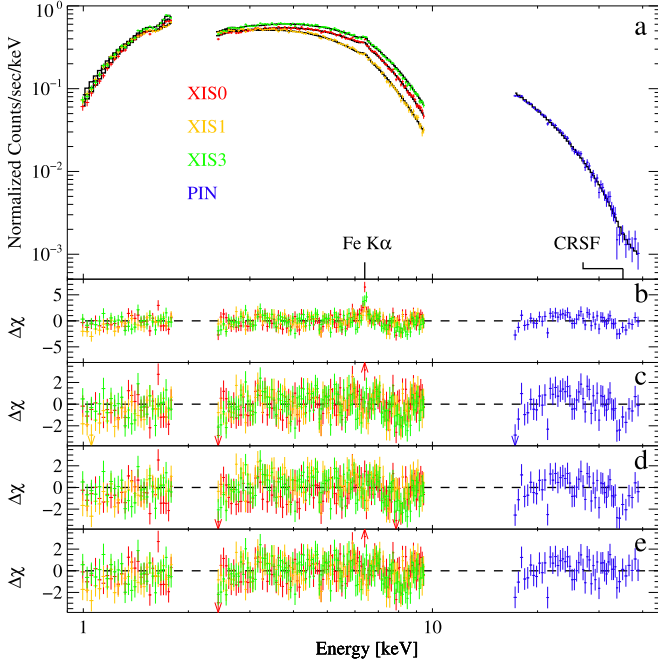


**Figure 5.** Spectra and best-fit model for XIS 0, 1, 3 (in red, yellow, and green, respectively) and PIN (in blue). The spectra were fitted simultaneously with the model described by Equation (10) with an FDCO continuum model. The bottom panels show the residuals as  $\Delta\chi$  obtained by (b) fitting only the continuum, (c) fitting the continuum with the Fe  $K\alpha$  line, (d) fitting the continuum with the Fe  $K\alpha$  line and the 35 keV CRSF feature with  $D_{\text{CRSF}}$  set to 0 after fitting, (e) fitting the continuum with the Fe  $K\alpha$  line and the 35 keV CRSF feature.

spectrum, but they do not provide a good description of the XIS spectrum (below 8 keV the spectra were variable between individual monitoring pointings).

Maitra & Paul (2013) reported *highcut* and *npex* fit of the same *Suzaku* data set. Their best-fit parameters are generally not consistent with ours. For example, their *highcut* cut-off energy of  $7.02^{+0.69}_{-0.29}$  keV and their *npex* positive power-law normalization are not consistent with 0. A possible explanation for this discrepancy is that the *highcut* model has a break at the cut-off energy, which here is located at the energy of the Fe K edge. In part this approach therefore could be modeling imperfections of the fit in the region of the iron line and edge. No edge component was required in our fits. Using the approach of Maitra & Paul (2013) by extending the spectrum to 70 keV, i.e., beyond where the source is detected (see next section), and allowing for a 9 keV wide cyclotron line using the *cyclabs* model we were able to reproduce their continuum parameters. Maitra & Paul (2013) do not quote flux calibration constants. We found a PIN/XIS ratio similar to our other fits. We also assumed that their unitless CRSF width values  $W_{\text{CRSF}}$  were given in keV. As mentioned in Section 1 a 9 keV wide cyclotron line can be expected to in part model the continuum (Müller et al. 2013b). Similar to Maitra & Paul (2013) we found that thermal Comptonization of soft photons in a hot plasma (*comptt*, Titarchuk 1994) cannot explain the *Suzaku* spectra, particularly in the PIN range ( $\chi^2_{\text{red}}/\text{dof} = 5.86/464$ , unconstrained parameters).

#### 4.2. Cyclotron Resonance Scattering Feature

The cyclotron line we found in the *Suzaku* spectrum from the end of the second outburst of the 2010 series has an energy of  $E_{\text{CRSF}} = 35.16^{+1.5}_{-1.3}$  keV, a line depth of  $D_{\text{CRSF}} = 2.42^{+1.5}_{-1.3}$  keV and a fixed width of  $\sigma_{\text{CRSF}} = 2$  keV. Heindl et al. (2001) found a CRSF with similar parameters at  $E_{\text{CRSF}} = 36.2^{+0.5}_{-0.7}$  keV with  $D_{\text{CRSF}} = 2.79^{+2.14}_{-1.77}$  keV ( $\tau_{\text{CRSF}} = 0.33^{+0.07}_{-0.06}$ ) and  $\sigma_{\text{CRSF}} = 3.37^{+0.92}_{-0.75}$  keV for the bright outburst in 1998, from *RXTE* data. The CRSF energy obtained with *RXTE* is consistent with the one obtained with *Suzaku*. Müller et al. (2012) did not find a

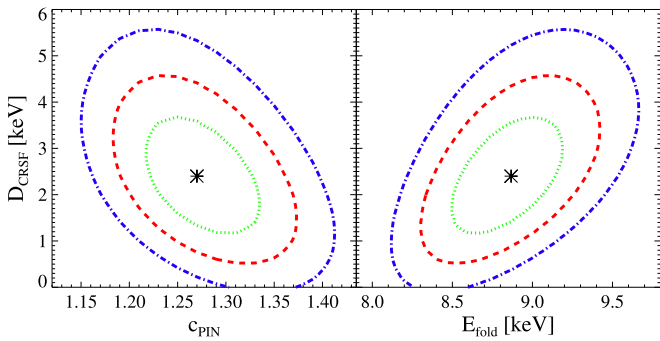


**Figure 6.** Confidence contour plots showing moderate correlations between the depth of the CRSF at 35 keV and the folding energy (top) and between the depth of the CRSF at 35 keV and the PIN flux cross-calibration constant (bottom) for the FDCUT III fit of Table 3. Contours for confidence levels of 1, 2, and  $3\sigma$  are shown in dotted green, dashed red, and dash-dotted blue, respectively.

line at 35 keV, but found marginal evidence ( $1.8\sigma$ ) for a CRSF at  $\sim 25$  keV in the first and third outbursts of the 2010 series.

In order to check the robustness of the *Suzaku* detection of an unresolved cyclotron line at 35 keV with respect to changes of the continuum model parameters we calculated confidence contours for two parameters of interest, the CRSF depth  $D_{\text{CRSF}}$  and one continuum parameter at a time. We found no strong correlations. Not unexpectedly, moderate correlations are present with the folding energy  $E_{\text{fold}}$  and with the flux cross-calibration constant of the PIN spectrum  $c_{\text{PIN}}$ , see Figure 6. The confidence contours indicate that the CRSF feature is present independently of the continuum modeling on a  $\sim 3\sigma$  level. We further confirmed this picture by determining a significance of  $2.81\sigma$  for a cyclotron line feature at 35 keV using Monte Carlo simulations. This significance value was obtained by simulating 5000 spectra based on the best-fit model parameters without the CRSF (column FDCUT II of Table 3) and fitting them with and without including the CRSF (width fixed at 2 keV in the former case). In 25 cases we found a bigger improvement in  $\chi^2$  than in the real data, resulting in the quoted significance. For an unresolved line at 25 keV we determined a  $3\sigma$  upper limit of  $D_{\text{CRSF}} \sim 0.9$  for the line depth, based on Monte Carlo simulations including a 25 keV line with different depths and for each depth comparing the  $\chi^2$  values obtained from fitting the line to the data and the simulations.

We also investigated the modeled PIN background spectrum and the effect of its uncertainty on the fit parameters, particularly of the cyclotron line. To this end we first included the background normalization as a fit parameter in the FDCUT III model using *recon*. The uncertainty of the fitted background normalization ranged from a decrease of 20% to an increase of 3%. Repeating the fit fixing the background normalization at either of these values or at the default and adding the expected systematic uncertainty of 3% to the PIN background spectrum (ISAS/JAXA & X-ray Astrophysics Laboratory NASA/Goddard Space Flight Center 2013, node10) did not significantly change the resulting cyclotron line parameters. We confirm Maitra & Paul (2013)’s report that the normalization of the background spectrum observed when the source was occulted by the Earth (obtained by setting  $\text{ELV} < -5^\circ$  in *aepipeline*) was about 20% below that of the modeled background spectrum. This result can qualitatively be explained with the anticorrelation between the magnetic field strength and the background flux at a given satellite

location (ISAS/JAXA & X-ray Astrophysics Laboratory NASA/Goddard Space Flight Center 2015, node12): A measure for the strength of the Earth’s magnetic field—the time-resolved magnetic cut-off rigidity of the Earth at the satellite position during the observation—can be obtained from the observation’s filter file and we found that it was on average lower during the on-source time ( $\text{ELV} > 5$ ) than during the Earth-occultation time ( $\text{ELV} < -5$ ) for the XTE J1946+274 observation.

In Section 3.2 we showed that there is no broadband detection of the pulsar above 40 keV. The background-subtracted spectrum generally confirms this. It is consistent with 0 above 38 keV with the exception of two independent spectral bins in the 43–47 keV range that show a marginal source detection (see also Figure 4 of Maitra & Paul 2013). The picture stays the same when taking the 3% background uncertainty into account. Using non-background-subtracted events we detected no pulsations in the 38–45 keV range and marginal ones in the 43–47 keV range, confirming again that the background model is sufficiently accurate. The background spectrum dominates over the source contribution above  $\sim 33$  keV and declines smoothly with energy with no systematic features around 35 or 40 keV. Above 38 keV the source spectrum might thus show some structure but it is mostly below the detection limit and was therefore excluded from our analysis.

## 5. DISCUSSION

### 5.1. Pulse Period Evolution and Orbit Parameters

We successfully applied the accretion torque theory of Ghosh & Lamb (1979) to XTE J1946+274 and updated the orbital solution for this source (Table 2). Previously Wilson et al. (2003) used three different approaches to model the observed pulse period evolution obtained by *RXTE*-PCA and *CGRO*-BATSE in 1998, which was dominated by a strong spin-up as well. Comparing the resulting orbital parameters to ours we find that the semimajor axis,  $a_{\text{sm}} \sin i$ , agrees best with their 10th-order polynomial model. Extrapolating our derived time of periastron passage,  $\tau$ , back to 1998, gives times which agree to within  $2\sigma$  with the result of their model as well. The orbital period,  $P_{\text{orb}}$ , and eccentricity,  $e$ , are consistent with their linear model, while the longitude of periastron,  $\omega$ , is the same as in their piecewise approximation within the uncertainties. As noted by Wilson et al., however, the  $\chi^2$  of all three different approaches is not acceptable because the models do “not completely describe the intrinsic torques.”

In contrast to other methods such as, e.g., a Fourier series approach (e.g., Kühnel et al. 2013), calculating the spin-up of accreting pulsars using the theory of Ghosh & Lamb (1979) allows us to model the possibly complex, intrinsic spin period evolution of the neutron star with better accuracy (see also Galloway et al. 2004; Sugizaki et al. 2015). As a result the orbital motion can be properly disentangled from the overall observed pulse period evolution and the derived orbital parameters are generally more reliable. We caution, however, that assuming  $P(t')$  is a constant on the right side of Equation (3) in order to simplify the calculation of this differential equation (see, e.g., Sugizaki et al. 2015) might lead to additional uncertainties when fitting longer time series. If we set  $P(t') = P_0$ , for example, the modeled pulse period evolution differs up to 0.01 ms, which is of the same order as the

uncertainties of the *Fermi*-GBM period measurements. As soon as more precise flux measurements are used for  $F(t)$  or the measured spin-up is even stronger than for XTE J1946+274 the differential equation should thus be solved properly.

This kind of timing analysis would not be possible without regular flux monitoring by all-sky observatories, such as *Fermi*-GBM, *Swift*-BAT, or MAXI.

### 5.2. Mass Function and Orbit Inclination

The accurately determined orbital parameters allow us to derive the value of the mass function of XTE J1946+274 following the same approach as in, e.g., Wilson et al. (2003). The mass function of a binary,

$$f(M) = \frac{(M_{\text{opt}} \sin i)^3}{(M_{\text{NS}} + M_{\text{opt}})^2} = \frac{4\pi^2 (a_{\text{sm}} \sin i)^3}{G P_{\text{orb}}^2} \quad (11)$$

depends on the masses,  $M_{\text{opt}}$  and  $M_{\text{NS}}$ , of the optical companion and neutron star, respectively, and on the orbital inclination angle,  $i$ . However, the mass function can also be calculated using the orbital period,  $P_{\text{orb}}$ , and the projected semimajor axis,  $a_{\text{sm}} \sin i$ . Using the orbital parameters listed in Table 2 we derive consistent values of  $f(M) = 3.77^{+0.11}_{-0.07} M_{\odot}$  for disk accretion and  $f(M) = 3.82^{+0.07}_{-0.07} M_{\odot}$  for wind accretion. Assuming the same mass range for the companion star of  $10 M_{\odot} \leq M_{\text{opt}} \leq 16 M_{\odot}$  as used by Wilson et al. (2003) and the canonical neutron star mass  $M_{\text{NS}} = 1.4 M_{\odot}$ , we can solve Equation (11) for the inclination angle,  $i$ . Using the widest possible range for the mass function as calculated above,  $3.70 M_{\odot} \leq f(M) \leq 3.89 M_{\odot}$ , we derive an orbital inclination angle of  $41^{\circ} \leq i \leq 52^{\circ}$ . This is in good agreement with the value of  $i \gtrsim 46^{\circ}$  as found by Wilson et al. (2003).

As already argued by Wilson et al. (2003), the inclination angle of the Be disk,  $i_{\text{disk}}$ , with respect to the observer is not necessarily aligned with the inclination angle of the orbit,  $i$ . From measurements of the width of the single-peaked  $H\alpha$  line in an optical spectrum, Wilson et al. (2003) concluded that the Be star is seen nearly pole-on. Thus, the Be disk and orbital plane might indeed be misaligned in XTE J1946+274. Özbey Arabacı et al. (2014) recently analyzed optical spectra of the system and noted, however, that deriving the Be-disk inclination from the  $H\alpha$  line profile is highly uncertain based on theoretical investigations by Silaj et al. (2010). Assuming that the orbital plane and the Be disk are aligned ( $i_{\text{disk}} = i$ ), Özbey Arabacı et al. (2014) derived the rotational velocity of the Be star. They concluded that the Be companion of XTE J1946+274 is rotating with 0.50–0.72 times the critical break-up velocity of a typical Be-type star ( $v_{\text{crit}} \sim 618 \text{ km s}^{-1}$ ). Using their initial value of the projected velocity,  $v \sin i = 323 \text{ km s}^{-1}$  and our determined inclination angle,  $i$ , we find a velocity of 0.66–0.80 times the break-up velocity.

### 5.3. Outburst Behavior

Two outburst series of XTE J1946+274 have been observed, one in 1998 (Wilson et al. 2003) and one in 2010 (Figure 1) with two to three outbursts per orbit. In order to explain this X-ray activity the companion of XTE J1946+274 has been studied in the optical and IR. Based on observations of permanent  $H\alpha$  emission, Özbey Arabacı et al. (2014) conclude that during X-ray quiescence a large Be disk is present. They

observed a brightening in the optical/IR indicating that the Be star experienced a long mass-ejection event from 2006 to 2012, reaching its maximum intensity in 2010, around the time of the outburst series. Özbey Arabacı et al. postulate that this ejection caused an increase in size, perturbations, and warping of the Be disk. They also state that the X-ray activity is triggered by the neutron star coming into contact with the warped areas in the tilted Be disk. This could explain why we observe two to three outbursts per orbit. The presence of  $H\alpha$  and optical/IR emissions after the X-ray activity indicates that once the material was consumed through accretion, the Be disk quickly and steadily recovered and the system returned to quiescence (Özbey Arabacı et al. 2014).

### 5.4. Continuum and Fe $K\alpha$ Line

We described the spectral shape of XTE J1946+274 with a Fermi–Dirac cut-off power law together with an Fe  $K\alpha$  fluorescence line and a CRSF at 35 keV. We find  $E_{\text{fold}} = 8.89$  (4) keV and a hydrogen column density of  $N_{\text{H}} = 1.67(3) \times 10^{22} \text{ cm}^{-2}$ . These parameters are roughly consistent with the ones found by Müller et al. (2012) in PCA data taken during earlier outbursts, namely  $E_{\text{fold}} = 6.0^{+2.6}_{-1.6} - 8.1^{+0.7}_{-0.6}$  keV, and  $N_{\text{H}} = 1.77^{+0.25}_{-0.29} - 5.1^{+2.5}_{-3.3} \times 10^{22} \text{ cm}^{-2}$ . Their measured  $\Gamma = 0.74^{+0.12}_{-0.17} - 1.04^{+0.13}_{-0.18}$  is slightly softer than ours,  $\Gamma = 0.57(2)$ . The cut-off energy is different as well: it is found here to be zero, while Müller et al. (2012) found  $E_{\text{cut}} = 14 \pm 4 - 19.4^{+2.1}_{-9.7}$  keV.

In order to study the changes in the spectral shape at different times and luminosities during the outburst series we compared our best-fit model and the models fitted in Müller et al. (2012) by eye. The *Suzaku* spectrum is harder at high energies ( $>12$  keV) than the spectra from Müller et al. (2012). This hardness change could be an indication of a higher temperature of the plasma in the accretion column, despite the lower luminosity. At first glance this may seem inconsistent, however, the electron temperature and mass accretion rate cannot be clearly determined without a physical continuum model. The implementation and testing of such a physical model is a work in progress (Marcu et al. 2014).

We and Müller et al. (2012) both find  $N_{\text{H}}$  values that are almost twice as large as the Galactic  $N_{\text{H}}$  in the direction of XTE J1946+274 ( $N_{\text{H}} = 9.4 \times 10^{21} \text{ cm}^{-2}$ ; Kalberla et al. 2005). This excess indicates the presence of absorbing material intrinsic to the X-ray binary system. The excitation of such neutral to moderately ionized material surrounding the neutron star by the X-rays emitted from the accretion column can produce fluorescent lines from iron and other elements. These lines are a very useful tool for analyzing the properties of the material (e.g., Inoue 1985; Leahy & Creighton 1993; Torrejón et al. 2010; Reig & Nespoli 2013).

We find a narrow ( $\sigma_{\text{Fe}} = 0.1$  keV) Fe  $K\alpha$  fluorescent emission line at  $E_{\text{Fe}} = 6.41(3)$  keV, confirming the presence of this neutral to moderately ionized material. The flux was  $A_{\text{Fe}} \sim 8.6 \times 10^{-5} \text{ photons cm}^{-2} \text{ s}^{-1}$  (see Table 3). The equivalent width is 32.2 eV for the *Suzaku* observation, consistent with the  $\sim 29$  eV found by Maitra & Paul (2013) in the same data set, but lower than the measured 49–69 eV found in earlier data taken at different fluxes (Heindl et al. 2001; Müller et al. 2012). As shown, e.g., by Inoue (1985), one expects the flux in the fluorescence line to be correlated with the continuum flux above 7 keV. Figure 7 shows this relationship using data of all published observations

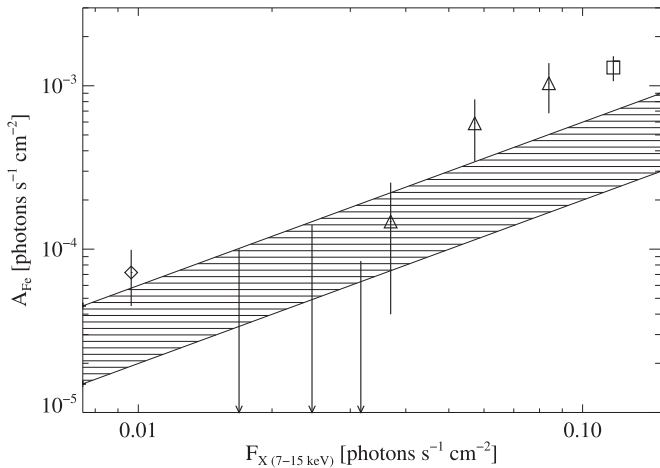


**Figure 7.** Flux of the Fe K $\alpha$  fluorescence line as a function of the 7–15 keV continuum flux. The diamond represents the *Suzaku*-XIS 0 data. All other data points are from Müller et al. (2012): triangles represent multiple instrument results from the first 2010 outburst (*RXTE*, *INTEGRAL*—two high-flux triangles) and from the third 2010 outburst (*Swift*, *RXTE*, *INTEGRAL*—two low-flux triangles and two upper limits), and the square corresponds to the *RXTE* average spectrum of the 1998 outburst. The hashed region describes the predicted correlation according to Nagase et al. (1986) calculated using  $N_{\text{H}}$  and continuum normalization values from the *Suzaku* spectral fit and the Müller et al. (2012) fits.

of XTE J1946+274, extending a similar figure by Müller et al. (2012) to lower fluxes. The figure also shows the correlation predicted by Equation (4a) of Nagase et al. (1986), which is an estimate for the fluorescent line flux as a function of  $N_{\text{H}}$  and continuum flux. The hashed region in Figure 7 illustrates the range of the expected Fe K $\alpha$  flux values according to Nagase et al. (1986), taking into account the variation in  $N_{\text{H}}$  between all published spectral fits. This range is an upper limit to the absorption column of the system. For the values with the lowest uncertainties the observed Fe K $\alpha$  flux is slightly higher than the one predicted by Nagase et al. (1986). This is especially the case for the high-flux data points and is qualitatively consistent with their higher equivalent width compared to the *Suzaku* measurement. A possible reason for this slight excess could be an overabundance of iron in the emitting medium. Alternatively, the excess could also be due to the fact that the ionization structure of the material is more complicated than the purely neutral Fe absorber assumed by Nagase et al. (1986). Finally, it is also likely that the emission is not purely from the line of sight, but from other areas such as fluorescence from a tilted and/or warped Be disk around the neutron star.

### 5.5. Cyclotron Resonance Scattering Feature

Evidence of a  $\sim 35$  keV cyclotron line was first seen by Heindl et al. (2001) in *RXTE* data obtained during a time when the source was much brighter than in the observations analyzed here. Our *Suzaku* observation supports the presence of this line: the  $\chi^2$  slightly improved from 557 to 545, corresponding to a significance of  $2.81\sigma$  (obtained using Monte Carlo simulations), between the FDCUT II and FDCUT III fits. Including this line improved the fits with the other continuum models as well. The centroid energy of  $35.2^{+1.5}_{-1.3}$  keV implies a surface magnetic field of  $B_{\text{NS}} = 3.1^{+0.1}_{-0.1}(1+z) \times 10^{12}$  G.

The CRSF parameters are independent of the continuum model. Furthermore, describing the PIN data only with the  $n_{\text{pex}}$  model, we obtain a good fit with  $\chi^2_{\text{red}} = 0.92$  for 50 dof,

for continuum parameters consistent with Heindl et al. (2001). Both the energy of the cyclotron line and its optical depth measured with *Suzaku* are within  $1\sigma$  of those measured with *RXTE*. Note, however, that due to spectral complexity below 10 keV the *RXTE* based  $n_{\text{pex}}$  values do not describe the broad band (XIS and PIN) *Suzaku* data.

We find a lower centroid energy for the CRSF than the effectively  $\sim 40$  keV previously reported for this data set by Maitra & Paul (2013). As explained in Section 4.2, their higher value could be due to in part modeling an artificial feature, as these authors include PIN data above 40 keV, where the source is mostly not detected.

Our spectrum is not consistent with the 25 keV feature discussed by Müller et al. (2012). We tried including a feature with their parameters and the  $\chi^2_{\text{red}}$  increased to 1.92. When the depth of this 25 keV feature was left free it became consistent with zero.

### 5.6. Accretion Column

It has recently been recognized that different types of correlations between the energy of the CRSF  $E_{\text{CRSF}}$  and the X-ray luminosity  $L_{\text{X}}$  are observed for accreting pulsars, probably reflecting different accretion states (Staubert et al. 2007). Studying these correlations allows us to derive constraints on the physical conditions in the accretion column. Becker et al. (2012) presented a model of the different accretion regimes and of how the height (i.e., the  $B$ -field and therefore  $E_{\text{CRSF}}$ ) of the region in the accretion column where the CRSF is produced changes with luminosity for the different regimes (see also Mushtukov et al. 2015): for supercritical sources ( $L_{\text{X}} \gtrsim L_{\text{crit}}$ ) radiation pressure in a radiative shock in the accretion column is the dominant decelerator for the material inside the accretion column. A source in this regime is expected to show a negative  $E_{\text{CRSF}}-L_{\text{X}}$  correlation, as observed for V 0332+53 (Mowlavi et al. 2006). For moderately subcritical sources ( $L_{\text{X}} \lesssim L_{\text{crit}}$ ) the radiation-dominated shock causes the initial deceleration, followed by Coulomb interactions below the shock, which bring the matter to a stop on the neutron star surface. Subcritical sources in this regime are expected to show a positive  $E_{\text{CRSF}}-L_{\text{X}}$  correlation, as observed for Her X-1 or GX 304-1 (Staubert et al. 2007; Klochkov et al. 2012). The expected relationship at even lower luminosities ( $L_{\text{X}} \lesssim L_{\text{Coul}}$ ), where the radiative shock and Coulomb interactions disappear, and the matter falls through a gas-mediated shock before hitting the stellar surface, is less clear. A 0535+26, for example, is a low-luminosity source that does not show any changes of  $E_{\text{CRSF}}$  in pulse averaged spectra with luminosity (Caballero et al. 2007, but see Müller et al. 2013a and Sartore et al. 2015).

Where does XTE J1946+274 fit into this picture? In Figure 8 we show the Coulomb luminosity  $L_{\text{Coul}}$  and the critical luminosity  $L_{\text{crit}}$  for a range of  $B$ -fields, i.e., cyclotron line energies (after Becker et al. 2012), separating the different accretion regimes. These luminosities depend, among other things, on the accretion geometry outside of the Afvén sphere where two cases are presented: disk and wind accretion. Overplotted are the gravitational redshift-corrected cyclotron line energies and 3–60 keV luminosities from Heindl et al. (2001) and our *Suzaku* analysis. We calculated the *Suzaku* luminosity using the unabsorbed flux measurement from the FDCUT III spectral fit. The CRSF energy is consistent within errors between 1998 and 2010, implying that the height of the CRSF emission region is similar for both observations. The

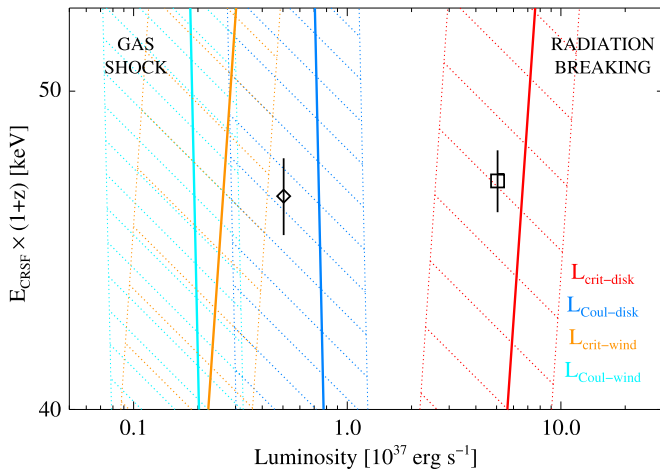


**Figure 8.** Relationship between the intrinsic CRSF energy and the luminosity of XTE J1946+274. The results of the spectral fits from this work (diamond) and Heindl et al. (2001) (square) are shown with respect to the Coulomb and critical luminosities (Equations (32) and (45) in Becker et al. 2012) of a neutron star with a standard mass and radius for the cases of disk (dark blue and red solid lines) and wind accretion (light blue and orange solid lines). The hashed luminosity ranges account for the uncertainty of the distance measurement.

luminosities, while both moderate, span a range larger than observed for any other moderate luminosity pulsar (e.g., Her X-1 or GX 304–1) and fall in the transition region between low and high luminosity pulsars. In the case of disk accretion, i.e., the default assumption for Be systems, both luminosities are consistent with subcritical accretion, with the 1998 *RXTE* measurement at  $L_X \lesssim L_{\text{crit}}$  and the *Suzaku* measurement at  $L_X \lesssim L_{\text{Coul}}$ . Taking the uncertainties of the distance measurement into account, the similarity of the cyclotron line energy measurements is not inconsistent with the Becker et al. (2012) picture. In the case of wind accretion XTE J1946+274 would have been supercritical during both measurements and a negative  $E_{\text{CRSF}}-L_X$  correlation would be expected. Calculating the difference in emission heights for supercritical accretion following Equation (40) of Becker et al. (2012) and assuming a dipole magnetic field,  $\Delta E_{\text{CRSF}} \lesssim 1.4$  keV is expected for the two luminosities. This is comparable to the uncertainties of the two  $E_{\text{CRSF}}$  measurements, i.e., though unlikely, we cannot rule out the presence of such a change. We note that wind accretion has so far only been discussed as a possibility for explaining the  $E_{\text{CRSF}}-L_X$  relationship of persistent, non-Be, low-luminosity sources like Vela X-1 and 4U 1538–522 (Fürst et al. 2014; Hemphill et al. 2014). We did not include the data from Müller et al. (2012) because the presence of a CRSF at 25 keV at fluxes between the 1998 and 2010 extremes is only marginally supported (see Section 4.2). However, a higher emission region at intermediate fluxes in the Coulomb braking regime (disk accretion) is again consistent with the Becker et al. (2012) picture, while it is not consistent in the supercritical regime (wind accretion). Using the more precise treatment of the critical luminosity by Mushtukov et al. (2015) is qualitatively in agreement with this picture.

We can calculate the CRSF emission region height for a subcritical source at which the Coulomb interactions start decelerating the plasma using Equation (51) of Becker et al.

(2012):

$$h_c = 1.48 \times 10^5 \text{ cm} \left( \frac{\lambda}{0.1} \right)^{-1} \left( \frac{\tau_*}{20} \right) \times \left( \frac{M_{\text{NS}}}{1.4 M_\odot} \right)^{19/14} \left( \frac{R_{\text{NS}}}{10 \text{ km}} \right)^{1/14} \cdot \left( \frac{B_{\text{NS}}}{10^{12} \text{ G}} \right)^{-4/7} \left( \frac{L_X}{10^{37} \text{ erg s}^{-1}} \right)^{-5/7} \quad (12)$$

where the following parameters are as defined in Becker et al. (2012):  $\lambda = 0.1$  describes the disk accretion case,  $\tau_* \sim 20$  is the Thomson optical depth in the Coulomb regime,  $M_{\text{NS}} = 1.4 M_\odot$  and  $R_{\text{NS}} = 10 \text{ km}$  are typical values for the neutron star mass and radius. We obtained  $h_c = 211 \text{ m}$  for the emission height using  $B_{\text{NS}} = 3.1(1+z) \times 10^{12} \text{ G}$  with  $z = 0.3$  and  $L_X = 5 \times 10^{37} \text{ erg s}^{-1}$  (Heindl et al. 2001).

The similarity of the observed pulse profiles at low and high fluxes supports a scenario where no strong changes in the emission geometry happen over and between outbursts. The 2010 *RXTE* and *Suzaku* pulse profiles of XTE J1946+274 are double-peaked with a deep and a shallow minimum that show weak energy dependence of the depths (Figure 3). This structure is strongly similar to what has been observed by Wilson et al. (2003) and Paul et al. (2001) during the 1998 outburst with other instruments at different luminosities. The source even shows a double-peaked profile during quiescence as observed by *Chandra* (Özbey Arabacı et al. 2014). Interestingly, the  $\sim 20\text{--}40$  keV pulse profile of A 0535+26 is very similar to that of XTE J1946+274 (Caballero et al. 2007; Sartore et al. 2015). Modeling the profiles of the 2005 August/September outburst of A 0535+26, Caballero et al. (2011) determined a possible emission pattern by taking into account the contribution of each of the two magnetic poles. They assumed a dipole magnetic field with axisymmetric emission regions. The asymmetry of the pulse profile minima is explained by a small offset of one of the emission regions from being antipodal. The profiles for A 0535+26 were obtained when the source had a luminosity of  $L_{3-50 \text{ keV}} \sim 0.8 \times 10^{37} \text{ erg s}^{-1}$  (Caballero et al. 2011), i.e., not unlike the lower range observed for XTE J1946+274.

In summary, for XTE J1946+274 the stability of the pulse profile shape, the lack of strong changes of the spectral shape (Section 5.4), and the possibly constant CRSF energy with luminosity all indicate that there have been no major changes in the accretion column structure and emission geometry over the broad range of moderate luminosities covered by observations.

## 6. SUMMARY AND CONCLUSIONS

In this paper we analyzed a 50 ks *Suzaku* observation of the accreting pulsar XTE J1946+274 taken at the end of the second outburst in an outburst series in 2010. We performed a detailed temporal and spectral analysis and compared our results to data available from other instruments and outbursts. In the following we summarize the results of our analysis.

1. We determined a new orbital solution based on *Fermi*-GBM and other data. Its parameters and possible intrinsic pulse period evolutions are listed in Table 2 and shown in Figure 4.

2. We observed no strong changes between the *Suzaku* spectrum and previously analyzed spectra for different luminosities and outbursts.
3. The *Suzaku* observation allowed us to extend the correlation between the continuum X-ray flux and the flux of the narrow Fe K $\alpha$  line to lower fluxes than observed before. Comparing the observed correlation with the theoretically expected values for fluorescence emission shows a possible slight elevation of the line flux. This could indicate either an overabundance of iron, a more complex ionization structure, or a more complex spatial structure of the emitting medium than assumed by the simplest model.
4. The *Suzaku* spectrum shows a feature that can be modeled with a cyclotron line component at  $35.2^{+1.5}_{-1.3}$  keV at a significance of  $2.81\sigma$ .
5. The unchanging cyclotron line energy and similar pulse profile shape with luminosity between 1998 and 2010 suggest that the source does not experience strong changes in emission geometry and that XTE J1946+274 has been consistently accreting in the subcritical regime.
6. There are similarities between XTE J1946+274 and A 0535+26 regarding their pulse profile structure and a possibly unchanging cyclotron energy with luminosity. A more detailed study of these similarities could prove useful for better understanding accreting X-ray pulsars in Be systems.

XTE J1946+274 is rarely in outburst, with its two known episodes of activity having occurred approximately a decade apart. It remains a source with many unanswered questions. In particular, monitoring of possible future outbursts with sensitive instruments such as the ones on *NuSTAR* or *Astro-H* could fill the gap in the cyclotron line energy versus X-ray luminosity correlation and shed new light on the accretion mechanism of this source.

D.M.M.-C. and K.P. acknowledge support by *Suzaku* NASA Guest Observer grant NNX11AD41G and NASA Astrophysical Data Analysis Program grant 12-ADAP12-0118. We acknowledge funding by the Bundesministerium für Wirtschaft und Technologie under Deutsches Zentrum für Luft- und Raumfahrt grants 50OR1113 and 50OR1207 and Deutsche Forschungsgemeinschaft grant WI 1860/11-1. We thank John E. Davis for the development of the SLXfig module, which was used to create Figure 4. M.T.W. and K.S.W. acknowledge support by the Chief of Naval Research and NASA Astrophysical Data Analysis Program grant 12-ADAP12-0118. V.G. acknowledges support by NASA through the Smithsonian Astrophysical Observatory (SAO) contract SV3-73016 to MIT for Support of the *Chandra* X-Ray Center (CXC) and Science Instruments. CXC is operated by SAO for and on behalf of NASA under contract NAS8-03060.

*Facilities:* *Suzaku*, *Fermi*, *RXTE*, *Swift*, *INTEGRAL*.

## REFERENCES

- Arnaud, K. A. 1996, in ASP Conf. Ser. 101, *Astronomical Data Analysis Software and Systems V*, ed. G. H. Jacoby & J. Barnes (San Francisco CA: ASP), 17
- Becker, P. A., Klochov, D., Schönherr, G., et al. 2012, *A&A*, 544, A123
- Boldt, E. 1987, in IAU Symp. 124, *Observational Cosmology*, ed. A. Hewitt, G. Burbidge, & L. Z. Fang (Cambridge: Cambridge Univ. Press), 611
- Caballero, I., Kraus, U., Santangelo, A., Sasaki, M., & Kretschmar, P. 2011, *A&A*, 526, A131
- Caballero, I., Kretschmar, P., Santangelo, A., et al. 2007, *A&A*, 465, L21
- Caballero, I., Pottschmidt, K., Bozzo, E., et al. 2010, *ATel*, 2692
- Campana, S., Israel, G., & Stella, L. 1999, *A&A*, 352, L91
- Coburn, W., Heindl, W. A., Rothschild, R. E., et al. 2002, *ApJ*, 580, 394
- Enoto, T., Makishima, K., Terada, Y., et al. 2008, *PASJ*, 60, 57
- Finger, M. H. 2010, *ATel*, 2847
- Fürst, F., Pottschmidt, K., Wilms, J., et al. 2014, *ApJ*, 780, 133
- Galloway, D. K., Morgan, E. H., & Levine, A. M. 2004, *ApJ*, 613, 1164
- Ghosh, P., & Lamb, F. K. 1979, *ApJ*, 232, 259
- Heindl, W. A., Coburn, W., Gruber, D. E., et al. 2001, *ApJL*, 563, L35
- Hemphill, P. B., Rothschild, R. E., Markowitz, A., et al. 2014, *ApJ*, 792, 14
- Illarionov, A. F., & Sunyaev, R. A. 1975, *A&A*, 39, 185
- Inoue, H. 1985, *SSRv*, 40, 317
- ISAS/JAXA & X-ray Astrophysics Laboratory NASA/Goddard Space Flight Center 2013, *The Suzaku Data Reduction Guide, Version 5*, <http://heasarc.gsfc.nasa.gov/docs/suzaku/analysis/abc/>
- ISAS/JAXA & X-ray Astrophysics Laboratory NASA/Goddard Space Flight Center 2015, *The Suzaku Technical Description*, [http://heasarc.gsfc.nasa.gov/docs/suzaku/prop\\_tools/suzaku\\_td/](http://heasarc.gsfc.nasa.gov/docs/suzaku/prop_tools/suzaku_td/)
- Kalberla, P. M. W., Burton, W. B., Hartmann, D., et al. 2005, *A&A*, 440, 775
- Klochov, D., Doroshenko, V., Santangelo, A., et al. 2012, *A&A*, 542, L28
- Koyama, K., Tsunemi, H., Dotani, T., et al. 2007, *PASJ*, 59, 23
- Krimm, H. A., Barthelmy, S. D., Baumgartner, W., et al. 2010, *ATel*, 2663
- Kühnel, M., Müller, S., Kreykenbohm, I., et al. 2013, *A&A*, 555, A95
- Leahy, D. A., & Creighton, J. 1993, *MNRAS*, 263, 314
- Leahy, D. A., Elsner, R. F., & Weisskopf, M. C. 1983, *ApJ*, 272, 256
- Maeda, Y. 2010a, *Photometry using the XIS-1 data taken with the narrow window modes*, Document JS-ISAS-SUZAKU-MEMO-2010-06, <ftp://legacy.gsfc.nasa.gov/suzaku/doc/xis/suzakumemo-2010-06.pdf>
- Maeda, Y. 2010b, *A possible flux variation of the XIS data taken after Dec. 18th, 2009*, Document JS-ISAS-SUZAKU-MEMO-2010-05, <ftp://legacy.gsfc.nasa.gov/suzaku/doc/xis/suzakumemo-2010-05.pdf>
- Maeda, Y. 2010c, *A possible pointing determination error between Dec. 18th, 2009 and June 15th, 2010*, Document JS-ISAS-SUZAKU-MEMO-2010-04, <ftp://legacy.gsfc.nasa.gov/suzaku/doc/xis/suzakumemo-2010-04.pdf>
- Maeda, Y., Someya, K., Ishida, M., et al. 2008, *Recent update of the XRT response. III. Effective Area*, Document JS-ISAS-SUZAKU-MEMO-2008-06, <http://www.astro.isas.jaxa.jp/suzaku/doc/suzakumemo/suzakumemo-2008-06.pdf>
- Maitra, C., & Paul, B. 2013, *ApJ*, 771, 96
- Marcu, D. M., Pottschmidt, K., Gottlieb, A. M., et al. 2014, in *Proc. of the 10th INTEGRAL Workshop, A Synergistic View of the High Energy Sky* (Trieste: SISSA), 065
- Mihara, T. 1995, Ph.D. thesis, Univ. Tokyo
- Mowlavi, N., Kreykenbohm, I., Shaw, S. E., et al. 2006, *A&A*, 451, 187
- Müller, D., Klochov, D., Caballero, I., & Santangelo, A. 2013a, *A&A*, 552, A81
- Müller, S., Ferrigno, C., Kühnel, M., et al. 2013b, *A&A*, 551, A6
- Müller, S., Kühnel, M., Caballero, I., et al. 2012, *A&A*, 546, A125
- Mushtukov, A. A., Suleimanov, V. F., Tsygankov, S. S., & Poutanen, J. 2015, *MNRAS*, 447, 1847
- Nagase, F., Hayakawa, S., Sato, N., Masai, K., & Inoue, H. 1986, *PASJ*, 38, 547
- Nowak, M. A., Hanke, M., Trowbridge, S. N., et al. 2011, *ApJ*, 728, 13
- Özbey Arabacı, M., Camero-Arranz, A., Gutierrez-Soto, J., et al. 2014, *A&A*, 582, 53
- Paul, B., Agrawal, P. C., Mukerjee, K., et al. 2001, *A&A*, 370, 529
- Reig, P., & Nespoli, E. 2013, *A&A*, 551, A1
- Sartore, N., Jourdain, E., & Roques, J.-P. 2015, *ApJ*, 806, 193
- Schwarzenberg-Czerny, A. 1989, *MNRAS*, 241, 153
- Silaj, J., Jones, C. E., Tycner, C., Sigut, T. A. A., & Smith, A. D. 2010, *ApJS*, 187, 228
- Smith, D. A., & Takeshima, T. 1998, *ATel*, 36
- Staubert, R., Shakura, N. I., Postnov, K., et al. 2007, *A&A*, 465, L25
- Suchy, S., Pottschmidt, K., Wilms, J., et al. 2008, *ApJ*, 675, 1487
- Sugizaki, M., Yamamoto, T., Mihara, T., Nakajima, M., & Makishima, K. 2015, *PASJ*, 67, 73
- Takahashi, T., Abe, K., Endo, M., et al. 2007, *PASJ*, 59, 35
- Tanaka, Y. 1986, in *IAU Coll. 89, Radiation Hydrodynamics in Stars and Compact Objects*, ed. D. Mihalas & K.-H. A. Winkler (Berlin: Springer), 198
- Titarchuk, L. 1994, *ApJ*, 434, 570
- Torrejón, J. M., Schulz, N. S., Nowak, M. A., & Kallman, T. R. 2010, *ApJ*, 715, 947
- Tsujiimoto, M., et al. 2010, *Anomaly of XIS0 in June 2009*, Document JS-ISAS-SUZAKU-MEMO-2010-01, <ftp://legacy.gsfc.nasa.gov/suzaku/doc/xis/suzakumemo-2010-01.pdf>
- Verner, D. A., & Yakovlev, D. G. 1995, *A&AS*, 109, 125
- Verrecchia, F., Israel, G. L., Negueruela, I., et al. 2002, *A&A*, 393, 983
- Wilms, J., Allen, A., & McCray, R. 2000, *ApJ*, 542, 914
- Wilson, C. A., Finger, M. H., Coe, M. J., & Negueruela, I. 2003, *ApJ*, 584, 996
- Wilson, C. A., Finger, M. H., Wilson, R. B., & Scott, D. M. 1998, *IAU Circ.*, 7014, 2